

High-resolution photoacoustic tomography of resting-state functional connectivity in the mouse brain

Mohammadreza Nasirivanaki^{a,1}, Jun Xia^{a,1}, Hanlin Wan^a, Adam Quentin Bauer^b, Joseph P. Culver^b, and Lihong V. Wang^{a,2}

^aOptical Imaging Laboratory, Department of Biomedical Engineering and ^bDepartment of Radiology, Washington University in St. Louis, St. Louis, MO 63130

Edited by Edward Ziff, New York University Medical Center, New York, NY, and accepted by the Editorial Board November 27, 2013 (received for review June 22, 2013)

The increasing use of mouse models for human brain disease studies presents an emerging need for a new functional imaging modality. Using optical excitation and acoustic detection, we developed a functional connectivity photoacoustic tomography system, which allows noninvasive imaging of resting-state functional connectivity in the mouse brain, with a large field of view and a high spatial resolution. Bilateral correlations were observed in eight functional regions, including the olfactory bulb, limbic, parietal, somatosensory, retrosplenial, visual, motor, and temporal regions, as well as in several subregions. The borders and locations of these regions agreed well with the Paxinos mouse brain atlas. By subjecting the mouse to alternating hyperoxic and hypoxic conditions, strong and weak functional connectivities were observed, respectively. In addition to connectivity images, vascular images were simultaneously acquired. These studies show that functional connectivity photoacoustic tomography is a promising, noninvasive technique for functional imaging of the mouse brain.

fcPAT | RSFC | mouse brain functional imaging | hyperoxia | hypoxia

Resting-state functional connectivity (RSFC) is an emerging neuroimaging approach that aims to identify low-frequency, spontaneous cerebral hemodynamic fluctuations and their associated functional connections (1, 2). Recent research suggests that these fluctuations are highly correlated with local neuronal activity (3, 4). The spontaneous fluctuations relate to activity that is intrinsically generated by the brain, instead of activity attributable to specific tasks or stimuli (2). A hallmark of functional organization in the cortex is the striking bilateral symmetry of corresponding functional regions in the left and right hemispheres (5). This symmetry also exists in spontaneous resting-state hemodynamics, where strong correlations are found interhemispherically between bilaterally homologous regions as well as intrahemispherically within the same functional regions (3). Clinical studies have demonstrated that RSFC is altered in brain disorders such as stroke, Alzheimer's disease, schizophrenia, multiple sclerosis, autism, and epilepsy (6–12). These diseases disrupt the healthy functional network patterns, most often reducing correlations between functional regions. Due to its task-free nature, RSFC imaging requires neither stimulation of the subject nor performance of a task during imaging (13). Thus, it can be performed on patients under anesthesia (14), on patients unable to perform cognitive tasks (15, 16), and even on patients with brain injury (17, 18).

RSFC imaging is also an appealing technique for studying brain diseases in animal models, in particular the mouse, a species that holds the largest variety of neurological disease models (3, 13, 19, 20). Compared with clinical studies, imaging genetically modified mice allows exploration of molecular pathways underlying the pathogenesis of neurological disorders (21). The connection between RSFC maps and neurological disorders permits testing and validation of new therapeutic approaches. However, conventional neuroimaging modalities cannot easily be applied to mice. For instance, in functional connectivity magnetic resonance imaging (fcMRI) (22), the resting-state brain activity is determined via the

blood-oxygen-level-dependent (BOLD) signal contrast, which originates mainly from deoxy-hemoglobin (23). The correlation analysis central to functional connectivity requires a high signal-to-noise ratio (SNR). However, achieving a sufficient SNR is made challenging by the high magnetic fields and small voxel size needed for imaging the mouse brain, as well as the complexity of compensating for field inhomogeneities caused by tissue–bone or tissue–air boundaries (24). Functional connectivity mapping with optical intrinsic signal imaging (fcOIS) was recently introduced as an alternative method to image functional connectivity in mice (3, 20). In fcOIS, changes in hemoglobin concentrations are determined based on changes in the reflected light intensity from the surface of the brain (3, 25). Therefore, neuronal activity can be measured through the neurovascular response, similar to the method used in fcMRI. However, due to the diffusion of light in tissue, the spatial resolution of fcOIS is limited, and experiments have thus far been performed using an exposed skull preparation, which increases the complexity for longitudinal imaging.

Photoacoustic imaging of the brain is based on the acoustic detection of optical absorption from tissue chromophores, such as oxy-hemoglobin (HbO₂) and deoxy-hemoglobin (Hb) (26, 27). This imaging modality can simultaneously provide high-resolution images of the brain vasculature and hemodynamics with intact scalp (28, 29). In this article, we perform functional connectivity photoacoustic tomography (fcPAT) to study RSFC in live mice under either hyperoxic or hypoxic conditions, as well as in dead mice. Our experiments show that fcPAT is able to detect

Significance

Clinical studies have demonstrated that resting-state functional connectivity (RSFC) is altered in many brain disorders. However, current RSFC imaging techniques cannot be easily applied to mice, the most widely used model species for human brain disease studies. Utilizing optical excitation and acoustic detection, we have developed a functional connectivity photoacoustic tomography (fcPAT) system, which allows noninvasive imaging of RSFC in the mouse brain, with a large field of view and high spatial resolution. In this article, we describe the unique strengths of fcPAT, as demonstrated by our experimental results. Considering the tremendous amount of brain research in mouse models, this work will elicit broad interest in many related fields.

Author contributions: L.V.W. designed research; M.N. and J.X. performed research; M.N., J.X., A.Q.B., and J.P.C. contributed new reagents/analytic tools; M.N. and J.X. analyzed data; and M.N., J.X., and H.W. wrote the paper.

The authors declare no conflict of interest.

Conflict of interest statement: L.V.W. has a financial interest in Microphotoacoustics, Inc. and Endra, Inc., which, however, did not support this work.

This article is a PNAS Direct Submission. E.Z. is a guest editor invited by the Editorial Board.

¹M.N. and J.X. contributed equally to this work.

²To whom correspondence should be addressed. E-mail: lhwang@seas.wustl.edu.

This article contains supporting information online at www.pnas.org/lookup/suppl/doi:10.1073/pnas.1311868111/-DCSupplemental.

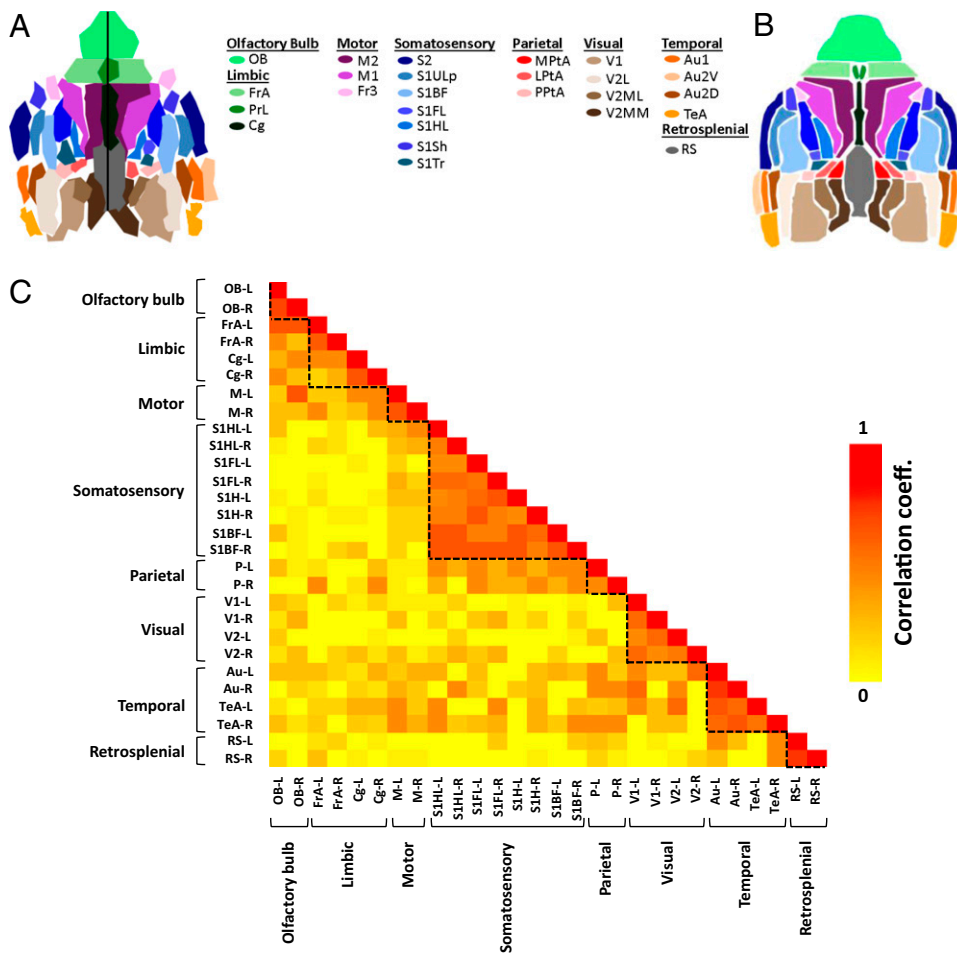


Fig. 4. Parcellation maps. (A) Parcellation map of the mouse described in Fig. 2. (B) Corresponding functional regions from the Paxinos histological atlas. (C) Correlation matrix between parcels in A. Each row and each column correspond to a parcel. Dashed lines were shown for added visualization. The letters L and R next to the dash stands for left and right, respectively. The regions and their sub-regions indicated in the atlas are as follows: Au, auditory cortex; Au1, primary auditory cortex; Au2V, secondary auditory–dorsal area; Au2D, secondary auditory–ventral area; Cg, cingulate; Fr3, frontal cortex area 3; FrA, frontal association; M1, primary motor cortex; M2, secondary motor cortex; M, motor cortex; MPtA, medial parietal association; OB, olfactory bulb; P, parietal region; PPtA, posterior parietal association; PrL, pre-limbic; RS, retrosplenial area; S1ULp, primary somatosensory–upper lips region; S1BF, primary somatosensory–barrel field; S1FL, primary somatosensory–forelimb region; S1HL, primary somatosensory cortex–hindlimb region; S1Sh, primary somatosensory–shoulder region; S1Tr, primary somatosensory cortex–trunk region; S2, secondary somatosensory; TeA, temporal association cortex; V1, primary visual cortex; V2, secondary visual cortex; V2MM, secondary visual cortex–mediomedial region; V2ML, secondary visual cortex–mediolateral region; V2L, secondary visual cortex–lateral region.

time. The 10-min temporal data were split into two 5-min datasets. The correlation maps produced from the two sets were similar (Fig. S94). We further confirmed the results by calculating the correlation coefficient between the maps from the first and second 5-min sections (Fig. S9B) and found the correlation coefficients to be greater than 0.78 for all of the seeds. This consistency suggests stable depth of anesthesia over the imaging duration. Although the connectivity maps were consistent and repeatable between multiple scans of the same mouse, the correlation maps (Fig. S3) and corresponding parcellation results (Fig. S6) varied slightly among mice. The differences were likely due to both dissimilarities in the positioning of the mouse head during setup and anatomical variations in the structural development of the mouse brains. These dissimilarities may also explain the differences in the size of the homotopic functional regions and their asymmetries. We also investigated the robustness of the algorithm to the choice of seed locations. Fig. S10 shows that seeds placed in different areas of the same region resulted in only slight differences in the RSFC maps.

In the parcellated image, most of the regions and subregions were evident. Regions such as the olfactory bulbs, motor and visual cortices, and retrosplenial and temporal regions were more pronounced in the parcellated image, whereas parcels were absent for some of the parietal and somatosensory subregions. This absence is possibly related to the size of the regions, with the larger regions being better able to tolerate variations in the locations of the brain structures.

RSFC during hypoxia was also studied. Through three periods of hyperoxia to hypoxia modulation, we consistently observed weaker correlations during hypoxia (Fig. 3 and Movie S2). Because the mouse was hypoxic for only 3 min during each modulation, a steady

recovery of functional connectivity was observed after restoration to hyperoxia. Because cerebral hypoxia is closely related to many brain and heart disorders, such as stroke and cardiac arrhythmia, RSFC can potentially be used to monitor the progression of these diseases and help prevent further damage to the brain (34, 35). This study may also allow neurologists to examine the order in which different functional regions lose their connectivities, and consequently to explore the region(s) necessary for survival.

Although MRI has been used for imaging RSFC in humans, it faces technical challenges in functional imaging of mice due to the smaller brains, which requires a high magnetic field (36). Thereby, early fMRI studies suspected that there is only unilateral correlation in the mouse brain (13). It was not until recently that Guilfoyle et al., with the susceptibility-induced distortion mitigated through interleaved echo planar imaging, were able to observe bilateral correlation in mouse brain using fMRI (36). However, they reported that bilateral correlation was only in a few regions and with poor RSFC resolution. In contrast, the fcPAT correlation maps shown in our study have much higher spatial resolution, which enables us to more accurately study the relation between the progression of the disease and alterations in RSFC.

Compared with fcOIS, fcPAT can simultaneously and non-invasively acquire vascular (37) and RSFC images at a high spatial resolution. Compared with other deeper tissue techniques such as functional connectivity diffuse optical tomography (fCDOT) (38) or functional connectivity Near Infrared Spectroscopy (fcNIRS) (39), fcPAT has orders of magnitude higher intrinsic imaging spatial resolution. In addition, with the wide variety of optical biomarkers, molecular imaging can also be performed using photoacoustic imaging (40). By combining high-resolution naturally coregistered

RSFC, vascular, and molecular images, fcPAT allows investigators to study the origin of RSFC and its underlying neurovascular coupling, as well as the genetics behind neurological disorders. With the growing use of mouse models for human neurological disease studies, such a technique meets a pressing need (29).

Although this study demonstrates the principle of fcPAT, future improvements can advance the technique. For instance, fast wavelength switching lasers are commercially available and can be used to accurately quantify the hemodynamics by spectrally separating the contributions of oxy- and deoxy-hemoglobin. By comparison, fcMRI cannot distinguish between increased blood oxygenation and decreased blood volume (23). Moreover, alternative RSFC signal processing methods such as independent component analysis (ICA) can be explored to complement and cross-validate the seed-based approach (41). Translation of fcPAT to large animals and humans is also possible, as photoacoustic techniques have been used successfully to image through monkey (42) and human skulls (43). Due to its low costs compared with fMRI, fcPAT should enable many laboratories that previously did not consider functional neuroimaging to contribute further to ongoing studies of human disease.

Methods

Imaging System. A Nd:YAG laser (Quantel, Brillant B) was used as the excitation source, at a pulse duration of 4–6 ns and a pulse repetition rate of 10 Hz (Fig. 1A). The laser beam was homogenized by an optical diffuser, resulting in a 2-cm-diameter beam on the surface of the mouse's head. The maximum light intensity at the surface was ~ 15 mJ/cm², which is below the American National Standards Institute limit of 20 mJ/cm² at 532 nm (the isobestic wavelength for HbO₂ and Hb) (44). The fcPAT signal is therefore directly proportional to the total hemoglobin concentration. The resulting photoacoustic signals were detected by a 5-cm-diameter, 512-element full-ring ultrasonic transducer array (Imasonic, Inc.). The array had an 80% bandwidth at a central frequency of 5 MHz. Within the 2-cm-diameter field of view, the system had an axial resolution of 100 μ m, a lateral resolution of 100–200 μ m, and an elevational resolution of 1.0 mm (30, 45). The photoacoustic signal was digitalized by a 64-channel data acquisition system, with a full-ring acquisition taking 1.6 s (28).

Mouse Preparation. For all of the experiments, 3–4-mo-old male Swiss Webster mice were used. Before imaging, the mouse was anesthetized with 2% (vol/vol) isoflurane at an air flow rate of 1.5L/min, and its hair was removed by a depilatory cream. The mouse was then secured to the imaging platform, and the cortex surface was positioned flat and lined up with the imaging plane. A mixture of 100 mg/kg ketamine and 10 mg/kg xylazine was then mixed and injected intraperitoneally. All experimental animal procedures were carried out according to the guidelines of the US National Institutes of Health, and all laboratory animal protocols were conducted as approved by the Animal Studies Committee of Washington University in St. Louis.

Image Reconstruction. Because the coverage of the ultrasonic transducer array was both closed and in-plane, the distribution of optical absorption could be accurately reconstructed using the universal back-projection algorithm. In this study, because only the similarity between different pixels' temporal traces was analyzed, the universal algorithm was simplified by back-projecting the detected pressure instead of its temporal derivative (46). This simplification also eliminated the need to deconvolve the transducers' electrical impulse responses, rendering images with a higher SNR.

Atlas Reconstruction. A horizontal-view atlas of the functional regions of the mouse brain was reconstructed from the coronal-view slices of the Paxinos atlas (5). Because the elevational resolution of the fcPAT system was about 1 mm, only structures located less than 1 mm below the surface were chosen for reconstruction of the atlas (Fig. 4B).

Image Preprocessing. In each experiment, 360 images of the mouse brain were acquired, using the fcPAT system over a span of 10 min. These images were first coregistered to the atlas shown in Fig. 4B to approximate the border of the brain and the locations of regions and subregions for seed placement. The landmarks used in the fcPAT vasculature image (Fig. 1B) for coregistration were the major blood vessels, including the inferior cerebral vein (between the olfactory bulb and frontal association), the superior sagittal sinus (between the left and right hemispheres of the olfactory

bulb, cingulate, and retrosplenial regions), the transverse sinus (between the cerebellum and colliculi areas, and the visual and auditory cortices), and the confluence of sinuses (intersection of the superior sagittal sinus and the transverse sinus). When necessary, the atlas was linearly transformed to match these landmarks, as the size and shape of the brain varies from mouse to mouse. After coregistration, regions not corresponding to the brain were assigned a pixel value of zero.

For optimal results, the images were then spatially smoothed using a Gaussian filter with a SD of 5 pixels (0.25 mm) truncated at a 10-pixel width (0.5 mm). The mean value of the temporal profile of each pixel was then subtracted. Because resting-state temporal fluctuation occurs only in the functional connectivity frequency range (0.009–0.08 Hz) (2, 3), a second-order, band-pass Butterworth filter with 3 dB cutoff frequencies of 0.009 Hz and 0.08 Hz was used to filter the temporal profiles. Finally, the global signal common to all pixels was subtracted from the temporal profile of each pixel, using a global regression method as previously described (32, 47, 48).

Fig. 54 C and D shows example frequency spectra of the time trace (temporal signal) acquired from the second motor cortex before and after processing, respectively. As expected, the processed signal contains primarily the functional connectivity frequencies (2, 3).

Seed-Based Analysis of Functional Connectivity. The functional connectivity maps were derived using a seed-based algorithm, which is widely used in resting-state connectivity studies due to its simplicity, sensitivity, and ease of interpretation (31, 32, 48–57). In this algorithm, seeds were manually selected in functional regions. Each seed's temporal trace was taken to be the average temporal trace of all points within a 5-pixel-diameter (250 μ m) disk. Pearson's correlation was then performed between the seed's temporal trace and that of each pixel in the image, resulting in a correlation map that showed functionally corresponding regions of the brain, both intra- and interhemispherically. Regions with high correlation values (strong correlation) between their corresponding time traces are likely to be functionally similar, whereas those with low correlation values (weak correlation) are likely to be functionally unrelated. In Fig. 51B, the time traces of the seeds in the left and right M2 regions are similar and therefore highly correlated. In contrast, the correlation between the time traces of seeds placed in the left somatosensory region and left or right M2 regions is low. Fig. 51C shows the correlation map obtained from the seed placed in the left secondary motor (M2) cortex.

Parcellation. The aim of the parcellation algorithm is to divide the surface of the brain into functional regions without user intervention (3). Cortical pixels with similar temporal traces are automatically grouped into the same functional region and coded with the same color, resulting in a map similar to the histological atlas shown in Fig. 4B. The similarity between temporal traces is determined according to the correlation to be explained in the following algorithm.

As shown in Fig. 55, the position of each functional region from the atlas was used as a starting point to define a probable functional region in the fcPAT images. This probable region was a disk centered at the corresponding center of the atlas, with a diameter equal to the longest length of that region in the atlas. The correlations of the time traces of the center pixel with each pixel in the probable region were calculated. For each pixel with a high correlation (correlation coefficient $r > 0.75$), a new correlation map was generated for the entire opposite hemisphere, using that pixel as the point of comparison. All such correlation maps were averaged and then Gaussian filtered. The Gaussian filter was centered in the corresponding probable region, with a FWHM equal to its diameter. To keep regions that could confidently be labeled as correlated, we applied thresholding. In the literature, different threshold values have been used: for example, 0.5, 0.6, and 0.7, where the maximum correlation coefficient is 1 (58–60). Following ref. 59, we chose 0.6 as the threshold ($P < 0.01$). The same value was used to threshold color bars in RSFC maps. Parcels with an area less than 200 pixels (0.5 mm²) were merged into the parcel nearest in Euclidian distance. Furthermore, parcels whose centers were more than 20 pixels (1 mm) away from the initial center of the probable region were eliminated. The values of 200 and 20 were chosen through empirical testing. All parcels were combined into a single image and color coded according to the atlas. To reduce user intervention, an automatic parcellation algorithm can be explored.

Paw Stimulation Procedure. In the stimulation experiment, each of the four paws was stimulated using needle electrodes inserted under the skin. The stimulation signal was pulsed with a 33% duty cycle at 1 Hz for 30 s at 1 mA. A 60-s recovery period was used between each set, and five such cycles were used for signal averaging (Fig. 57). The acquired images were then averaged over the periods with stimuli (I_s) and without stimuli (I_{ns}), and a relative intensity image was computed pixel by pixel using $(I_s - I_{ns})/I_{ns}$.

ACKNOWLEDGMENTS. The authors acknowledge and thank Dr. Joon Mo Yang for his help with figures. We also thank Profs. James Ballard and Sandra Matteucci for their close review of the article. This work was sponsored in

part by National Institutes of Health (NIH) Grants DP1 EB016986 (NIH Director's Pioneer Award), R01 EB008085, R01 CA134539, R01 CA159959, U54 CA136398, R01 EB010049, and R01 CA157277.

1. Biswal B, Yetkin FZ, Haughton VM, Hyde JS (1995) Functional connectivity in the motor cortex of resting human brain using echo-planar MRI. *Magn Reson Med* 34(4):537–541.
2. Fox MD, Raichle ME (2007) Spontaneous fluctuations in brain activity observed with functional magnetic resonance imaging. *Nat Rev Neurosci* 8(9):700–711.
3. White BR, et al. (2011) Imaging of functional connectivity in the mouse brain. *PLoS ONE* 6(1):e16322.
4. Kalthoff D, Seehafer JU, Po C, Wiedermann D, Hoehn M (2011) Functional connectivity in the rat at 11.7 T: Impact of physiological noise in resting state fMRI. *Neuroimage* 54(4):2828–2839.
5. Paxinos G, Franklin K (2003) *The Mouse Brain in Stereotaxic Coordinates: Compact* (Academic, San Diego), 2nd Ed.
6. Buckner RL, et al. (2009) Cortical hubs revealed by intrinsic functional connectivity: Mapping, assessment of stability, and relation to Alzheimer's disease. *J Neurosci* 29(6):1860–1873.
7. Seeley WW, Crawford RK, Zhou J, Miller BL, Greicius MD (2009) Neurodegenerative diseases target large-scale human brain networks. *Neuron* 62(1):42–52.
8. Varoquaux G, Baronnet F, Kleinschmidt A, Fillard P, Thirion B (2010) Detection of brain functional-connectivity difference in post-stroke patients using group-level covariance modeling. *Med Image Comput Comput Assist Interv* 13(Pt 1):200–208.
9. Lawrie SM, et al. (2002) Reduced frontotemporal functional connectivity in schizophrenia associated with auditory hallucinations. *Biol Psychiatry* 51(12):1008–1011.
10. Lowe MJ, et al. (2002) Multiple sclerosis: Low-frequency temporal blood oxygen level-dependent fluctuations indicate reduced functional connectivity initial results. *Radiology* 224(1):184–192.
11. Koshino H, et al. (2005) Functional connectivity in an fMRI working memory task in high-functioning autism. *Neuroimage* 24(3):810–821.
12. Waites AB, Briellmann RS, Saling MM, Abbott DF, Jackson GD (2006) Functional connectivity networks are disrupted in left temporal lobe epilepsy. *Ann Neurol* 59(2):335–343.
13. Jonckers E, Van Audekerke J, De Visscher G, Van der Linden A, Verhoye M (2011) Functional connectivity fMRI of the rodent brain: Comparison of functional connectivity networks in rat and mouse. *PLoS ONE* 6(4):e18876.
14. Vincent JL, et al. (2007) Intrinsic functional architecture in the anaesthetized monkey brain. *Nature* 447(7140):83–86.
15. Fransson P, et al. (2007) Resting-state networks in the infant brain. *Proc Natl Acad Sci USA* 104(39):15531–15536.
16. Smyser CD, et al. (2010) Longitudinal analysis of neural network development in preterm infants. *Cereb Cortex* 20(12):2852–2862.
17. Boly M, et al. (2009) Functional connectivity in the default network during resting state is preserved in a vegetative but not in a brain dead patient. *Hum Brain Mapp* 30(8):2393–2400.
18. Vanhaudenhuyse A, et al. (2010) Default network connectivity reflects the level of consciousness in non-communicative brain-damaged patients. *Brain* 133(Pt 1):161–171.
19. Liu Y, et al. (2008) Regional homogeneity, functional connectivity and imaging markers of Alzheimer's disease: A review of resting-state fMRI studies. *Neuropsychologia* 46(6):1648–1656.
20. Bero AW, et al. (2012) Bidirectional relationship between functional connectivity and amyloid- β deposition in mouse brain. *J Neurosci* 32(13):4334–4340.
21. Cazzin C, Ring CJA (2010) "Recent advances in the manipulation of murine gene expression and its utility for the study of human neurological disease. *Biochim Biophys Acta* 1802(10):796–807.
22. Buckner RL, Krienen FM, Yeo BT (2013) Opportunities and limitations of intrinsic functional connectivity MRI. *Nat Neurosci* 16(7):832–837.
23. Steinbrink J, et al. (2006) Illuminating the BOLD signal: Combined fMRI-fNIRS studies. *Magn Reson Imaging* 24(4):495–505.
24. Benveniste H, Blackband S (2002) MR microscopy and high resolution small animal MRI: Applications in neuroscience research. *Prog Neurobiol* 67(5):393–420.
25. Bahar S, Suh M, Zhao M, Schwartz TH (2006) Intrinsic optical signal imaging of neocortical seizures: The 'epileptic dip' *Neuroreport* 17(5):499–503.
26. Wang LV (2008) Tutorial on photoacoustic microscopy and computed tomography. *IEEE J* 14(1):171–179.
27. Yang JM, et al. (2012) Simultaneous functional photoacoustic and ultrasonic endoscopy of internal organs in vivo. *Nat Med* 18(8):1297–1302.
28. Gamelin J, et al. (2009) A real-time photoacoustic tomography system for small animals. *Opt Express* 17(13):10489–10498.
29. Yao J, et al. (2013) Noninvasive photoacoustic computed tomography of mouse brain metabolism in vivo. *Neuroimage* 64:257–266.
30. Xia J, et al. (2011) Three-dimensional photoacoustic tomography based on the focal-line concept. *J Biomed Opt* 16(9):090505.
31. Fox MD, et al. (2005) The human brain is intrinsically organized into dynamic, anticorrelated functional networks. *Proc Natl Acad Sci USA* 102(27):9673–9678.
32. Fox MD, Zhang D, Snyder AZ, Raichle ME (2009) The global signal and observed anticorrelated resting state brain networks. *J Neurophysiol* 101(6):3270–3283.
33. Laufer J, Zhang E, Raivich G, Beard P (2009) Three-dimensional noninvasive imaging of the vasculature in the mouse brain using a high resolution photoacoustic scanner. *Appl Opt* 48(10):D299–D306.
34. Puleria MR, et al. (1998) Apoptosis in a neonatal rat model of cerebral hypoxia-ischemia. *Stroke* 29(12):2622–2630.
35. Corday E, Irving DW (1960) Effect of cardiac arrhythmias on the cerebral circulation. *Am J Cardiol* 6:803–808.
36. Guilfoyle DN, et al. (2013) Functional connectivity fMRI in mouse brain at 7T using isoflurane. *J Neurosci Methods* 214(2):144–148.
37. Wang X, Pang Y, Ku G, Stoica G, Wang LV (2003) Three-dimensional laser-induced photoacoustic tomography of mouse brain with the skin and skull intact. *Opt Lett* 28(19):1739–1741.
38. White BR, et al. (2009) Resting-state functional connectivity in the human brain revealed with diffuse optical tomography. *Neuroimage* 47(1):148–156.
39. Mesquita RC, Franceschini MA, Boas DA (2010) Resting state functional connectivity of the whole head with near-infrared spectroscopy. *Biomed Opt Express* 1(1):324–336.
40. Wang LV, Hu S (2012) Photoacoustic tomography: In vivo imaging from organelles to organs. *Science* 335(6075):1458–1462.
41. White BR, Liao SM, Ferradal SL, Inder TE, Culver JP (2012) Bedside optical imaging of occipital resting-state functional connectivity in neonates. *Neuroimage* 59(3):2529–2538.
42. Yang X, Wang LV (2008) Monkey brain cortex imaging by photoacoustic tomography. *J Biomed Opt* 13(4):044009–044009, 5.
43. Nie L, et al. (2012) Photoacoustic tomography through a whole adult human skull with a photon recycler. *J Biomed Opt* 17(11):110506–110506.
44. Standard A (1993) *Z136. 1. American National Standard for the Safe Use of Lasers* (American National Standards Institute Inc, New York).
45. Xia J, et al. (2012) Whole-body ring-shaped confocal photoacoustic computed tomography of small animals in vivo. *J Biomed Opt* 17(5):050506.
46. Xu M, Wang LV (2005) Universal back-projection algorithm for photoacoustic computed tomography. *Phys Rev E Stat Nonlin Soft Matter Phys* 71(1 Pt 2):016706.
47. Murphy K, Birn RM, Handwerker DA, Jones TB, Bandettini PA (2009) The impact of global signal regression on resting state correlations: Are anti-correlated networks introduced? *Neuroimage* 44(3):893–905.
48. Fox MD, Greicius M (2010) Clinical applications of resting state functional connectivity. *Front Syst Neurosci* 4:19.
49. Damoiseaux JS, Greicius MD (2009) Greater than the sum of its parts: A review of studies combining structural connectivity and resting-state functional connectivity. *Brain Struct Funct* 213(6):525–533.
50. Birn RM, et al. (2008) The effect of respiration variations on independent component analysis results of resting state functional connectivity. *Hum Brain Mapp* 29(7):740–750.
51. Fox MD, Snyder AZ, Zacks JM, Raichle ME (2006) Coherent spontaneous activity accounts for trial-to-trial variability in human evoked brain responses. *Nat Neurosci* 9(1):23–25.
52. Rombouts SA, Stam CJ, Kuijter JP, Scheltens P, Barkhof F (2003) Identifying confounds to increase specificity during a "no task condition". Evidence for hippocampal connectivity using fMRI. *Neuroimage* 20(2):1236–1245.
53. Fransson P (2005) Spontaneous low-frequency BOLD signal fluctuations: An fMRI investigation of the resting-state default mode of brain function hypothesis. *Hum Brain Mapp* 26(1):15–29.
54. Laufs H, et al. (2003) Electroencephalographic signatures of attentional and cognitive default modes in spontaneous brain activity fluctuations at rest. *Proc Natl Acad Sci USA* 100(19):11053–11058.
55. Vincent JL, et al. (2006) Coherent spontaneous activity identifies a hippocampal-parietal memory network. *J Neurophysiol* 96(6):3517–3531.
56. Hampson M, Peterson BS, Skudlarski P, Gatenby JC, Gore JC (2002) Detection of functional connectivity using temporal correlations in MR images. *Hum Brain Mapp* 15(4):247–262.
57. Fox MD, Corbetta M, Snyder AZ, Vincent JL, Raichle ME (2006) Spontaneous neuronal activity distinguishes human dorsal and ventral attention systems. *Proc Natl Acad Sci USA* 103(26):10046–10051.
58. Biswal BB, Van Kylen J, Hyde JS (1997) Simultaneous assessment of flow and BOLD signals in resting-state functional connectivity maps. *NMR Biomed* 10(4-5):165–170.
59. Goulas A, Uylings HB, Stiers P (2012) Unravelling the intrinsic functional organization of the human lateral frontal cortex: A parcellation scheme based on resting state fMRI. *J Neurosci* 32(30):10238–10252.
60. Ng L, et al. (2009) An anatomic gene expression atlas of the adult mouse brain. *Nat Neurosci* 12(3):356–362.